International Journal of Heat and Technology
Vol. 43, No. 6, December, 2025, pp. 2291-2302
Journal homepage: http://iieta.org/journals/ijht

Thermo-Fluid Coupling in Eccentrically Heated Circular Enclosures: A Conjugate Convection Study

Feldji Kaltouma[1], Benachour Elhadj[1], Hasnat Mohammed[1], Nehila Tarek[1*], Asnoune Khadidja[2], Elmir Mohammed[1]

[1] Laboratory of Energy in Arid Regions (ENERGARID), Tahri Mohamed University of Bechar, Béchar 08000, Algeria
[2] Laboratory of Smart Grids and Renewable Energies, Tahri Mohamed University of Bechar, Béchar 08000, Algeria

Corresponding Author Email: nehila.tarek@univ-bechar.dz

https://doi.org/10.18280/ijht.430627

Received: 6 October 2025
Revised: 17 November 2025
Accepted: 24 November 2025
Available online: 31 December 2025

Keywords:
cylindrical flow, conjugate heat transfer, eccentric circular crown heat source, Bejan number, high-conductivity insert

ABSTRACT

This work presents a detailed numerical investigation of conjugate natural convection in a square cavity containing an eccentric circular copper crown heat source. The steady, incompressible Navier–Stokes and energy equations are solved using the finite element method. The analysis emphasizes thermo-fluid interactions at the fluid–solid interface and the impact of geometric asymmetry on flow and thermal fields. At moderate eccentricity (E = 1/4), coherent vortex structures and nearly symmetric isotherm plumes enhance fluid mixing and sustain high Nusselt numbers. Under strongly convective conditions ($Ra = 10^7$), the average Nusselt number decreases by nearly 50% for E = 1 compared to E = 1/4, while local Nusselt number peaks become concentrated near stagnation zones, indicating uneven heat transfer across the interface. Entropy generation analysis and the Bejan number are presented over angular positions ranging from 0° to 360°, revealing that the angular shift of entropy generation peaks reflects asymmetry effects of up to ~33%. The findings demonstrate that increased eccentricity weakens convective strength, reducing stream function magnitudes by approximately 35%. A new empirical correlation is proposed to predict the average Nusselt number as a function of the eccentricity ratio and Ra number. The results reveal that excessive eccentricity undermines thermo-fluid coupling, increases entropy generation, and significantly reduces heat transfer efficiency.

1. INTRODUCTION

Natural convection within enclosures continues to be a central topic in thermal sciences due to its fundamental role in applications such as solar energy harvesting, electronic device cooling, thermal energy storage, and HVAC systems. Among the various passive strategies employed to enhance thermal performance, geometric eccentricity, the deliberate displacement of a heat source or boundary from the geometric center, has emerged as an effective means to reshape flow structures and improve heat transfer rates.

A substantial body of experimental and numerical research has demonstrated that eccentricity can strongly influence convective behavior. For instance, Eid et al. [1] reported that both lateral and vertical eccentricities in elliptical annuli could enhance heat transfer by up to 40% compared to concentric configurations. Similarly, Wang [2] validated this sensitivity through combined experimental and numerical investigations in horizontal annuli. Azzawi et al. [3] further showed that the heat transfer coefficient is significantly affected by the eccentricity ratio, angular alignment, and Rayleigh number, with observed enhancements reaching 10%. In porous media, eccentric configurations introduce additional complexity. Mota et al. [4] demonstrated that certain eccentric geometries in saturated horizontal annuli may trigger multicellular flow patterns, which can reduce thermal transport—an important consideration in insulation design. Gholamalipour et al. [5] analyzed Cu–water nanofluids in porous annuli and found that optimal eccentricity enhances heat transfer and minimizes entropy generation, depending on Rayleigh and Darcy numbers. Kiwan and Alzahrany [6] present the effect of using porous inserts on natural convection heat transfer between two concentric vertical cylinders. It is found that the heat transfer characteristics can be strongly affected by the presence of porous inserts. Ait Messaoudene et al. [7] emphasized the interplay between eccentricity and fluid rheology, showing that both factors significantly shape thermal stratification and flow patterns in annular ducts—key for controlling industrial heat flows. Eccentricity has also been extensively examined in rotating systems.

Yoo [8] found that the Mixed convection of air between two horizontal concentric cylinders improves energy efficiency in a cooled rotating outer cylinder may suppress heat transfer. Guy and Stella [9] reported that the horizontal eccentricity of the inner cylinder gives, in contrast with known numerical results, a nonzero azimuthal flow rate in the channel between the two cylinders and substantially alters the thermal field and the geometry of the plume, Qiao et al. [10] showed that while eccentricity increases flow velocity, it compromises thermal uniformity—an important design trade-off in rapid cooling

systems.

In finned enclosures, the combination of eccentricity with structural enhancements yields dramatic performance gains. Ashouri et al. [11] and Taha et al. [12] applied a 3D lattice Boltzmann flux solver to simulate natural convection in eccentric horizontal annuli with perforated fins. Their results showed modest gains (~5.2%) with inner cylinder eccentricity and substantial improvement (up to 91.7%) with negatively offset eccentric fins. Recycling areas are often characterized by streamlined lines, heavily influenced by the presence of flexible fins and undulating walls. The fin has proven to play a vital role in fluid movement, allowing for rapid and significant convection [13]. Al-Mashat et al. [14] provided experimental evidence that both eccentricity ratio and angular orientation significantly influence heat transfer, achieving up to 10% enhancement over concentric designs. Application-specific investigations underscore the engineering relevance of eccentricity. Yoon and Shim [15] categorized natural convection regimes in square cavities with embedded eccentric cylinders, highlighting the evolution of flow and thermal fields with increasing offset.

Onochin and Jaszczur [16] show that moderate eccentricity can be tolerated in long-term operation without significant efficiency loss. Yang and Farouk [17] showed that eccentric rotating cylinders enhance local mixing and increase Nusselt numbers. Bejan and Lorente [18], adopting a constructal approach, established that asymmetric geometries—including eccentric designs—optimize thermal flow architecture. In geometrically complex systems, Roy et al. [19] revealed pronounced isotherm distortion and flow asymmetry due to eccentricity in square cavities with embedded cylinders, especially at high Rayleigh numbers. Similarly, Sheikholeslami et al. [20] studied nanofluid convection under magnetic fields and found that both magnetic field strength and eccentric offset jointly optimize thermal behavior. Micro- and mini-scale systems are also affected.

El-Shaarawi et al. [21] present results that are not available in the literature for the problem of conjugate laminar free convection in open-ended vertical eccentric annular channels, where the geometry effects have been investigated by considering fluid annuli having radius ratios NR2 = 0.1 and 0.3, 0.5 and 0.7, and four values of the eccentricity E = 0.1, 0.3, 0.5 and 0.7.

The objective of the study of Kurnia et al. [22] is to numerically investigate heat transfer and entropy generation in a double pipe helical heat exchanger with various cross-sections. Liu and Tao [23] numerically explored melting and solidification in PCM-filled eccentric shell-and-tube heat storage units. Their findings indicate that a downward eccentricity (E = –0.6) reduces melting time by 29.8% but hinders solidification. The best overall performance was observed at E = –0.2, reducing the total cycle time by 11.1%. Boulechfar et al. [24] analyzed porous elliptical annuli and confirmed that increasing eccentricity boosts equivalent thermal conductivity. Khaoula and Fayçal [25] examined mixed convection in eccentric horizontal annuli with rotating inner cylinders and found that small eccentricities paired with high Rayleigh numbers enhance thermal performance, though excessive rotation suppresses it. Humaira Tasnim et al. [26] highlighted the importance of aspect ratio and eccentricity in determining flow structure in cavity-embedded cylinders. Lastly, Zhang and Li [27] demonstrated that eccentric helically coiled tube-in-tube heat exchangers significantly improve Nusselt number distribution, validating eccentricity as an effective strategy for compact thermal system optimization. In summary, geometric eccentricity has proven to be a powerful passive control parameter, capable of enhancing convective flow patterns, boosting heat transfer performance, and reducing entropy generation across diverse configurations.

2. METHODOLOGY

2.1 Physical and mathematical modeling

The physical configurations investigated in this study capture the essential characteristics of heat transfer phenomena encountered in engineering applications and serve as a benchmark for assessing thermal and flow behavior in geometrically asymmetric domains Figure 1.

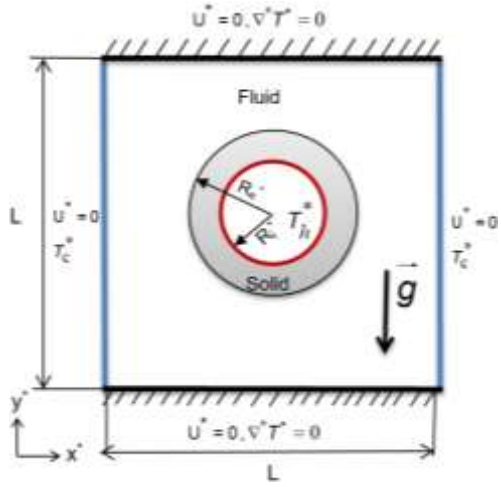

Figure 1. Schematic of the physical model

The system is modeled as two-dimensional, comprising a square cavity of side length L, with the left and right walls maintained at a uniform cold temperature T_C^* and the top and bottom walls treated as adiabatic, enforcing zero heat flux.

A central feature of the configuration is a geometrically eccentric, crown-shaped heat source defined by an inner radius R_i^* and outer radius $R_e^* = 2R_i^*$. Eccentricity is introduced by offsetting the center of the inner circle by a distance d^* to the right of the cavity's geometric center, inducing controlled asymmetry. The eccentricity ratio E, based on the relative displacement between centers, is treated as a key parameter and detailed in Figure 2. The crown's inner surface at R_i^* is maintained at a constant high temperature T_h^*, driving natural convection within the enclosure.

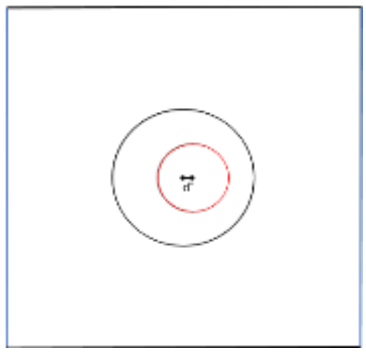

(a) E = 1/4

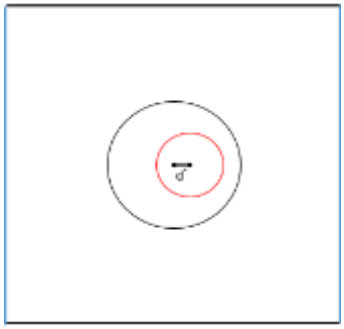

(b) E = 1/2

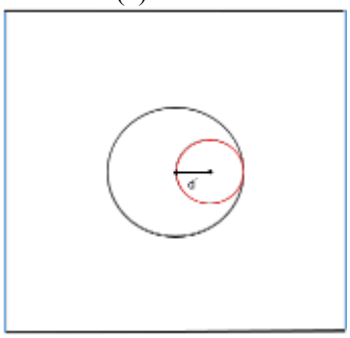

(c) E = 1

Figure 2. Schematic of the eccentric circular crown for different eccentricity ratios: (a) E = 1/4, (b) E = 1/2, (c) E = 1

In our simulation, we assume a realistic scenario: a smooth, non-compressible flow of a standard fluid. The fluid's heat-related properties remain constant, except for its density, which changes with temperature, influencing buoyancy—a simplification that boosts efficiency without sacrificing accuracy, suitable for the temperature ranges we're examining.

We use time-dependent equations to describe the system, covering mass, momentum, and energy conservation for both the fluid and solid parts. For the fluid, we model how heat spreads, moves with the flow, and is affected by buoyancy. For the solid copper crown, heat transfer occurs solely through conduction. At the boundary between the fluid and the crown, we ensure a seamless transfer of heat by matching their temperatures and heat flows.

The application of air as a reference fluid is not consistently systematic; in some cases, it is substituted with nanoparticles, a practice occasionally required on a large scale as demonstrated in the study by Benameur et al. [28].

This integrated approach provides a robust method for studying how natural convection and heat conduction interact within asymmetrically shaped enclosures.

2.2 Dimensionless formulation

To generalize the analysis and enhance computational efficiency, the governing equations are nondimensionalized using the following dimensionless variables and parameters:

$$\begin{aligned} &\left(R_i, R_e\right)=\frac{\left(R_i^*, R_e^*\right)}{L}, U=\frac{u^* L E}{\alpha_f}, \nabla=\nabla^* . L \\ &T=\frac{T^*-T_c^*}{T_h^*-T_c^*}, t=\frac{t^* \alpha_f}{L^2}, P=\frac{P^* L^2}{\rho_f \alpha_f^2}, \\ &\mathrm{D}=\frac{L^2 E}{\alpha_f \mu_f} \mathrm{D}^*, \sigma=\frac{L^2}{\rho_f \alpha_f^2} \sigma^* \end{aligned} \tag{1}$$

The key dimensionless groups governing the thermo-fluid behavior are:

$$Ra=\frac{g_y \beta\left(T_h-T_c\right) L^3}{\alpha_f \upsilon_f}, \mathrm{Pr}=\frac{\upsilon_f}{\alpha_f}, \quad \alpha_r=\frac{\alpha_s}{\alpha_f} \tag{2}$$

where, Ra and Pr denote the Rayleigh and Prandtl numbers, respectively, and α_r is the thermal diffusivity ratio between the solid and fluid domains.

Substituting the dimensionless variables into the governing equations yields the nondimensional forms:

- **Continuity**

$$\nabla . U=0 \tag{3}$$

where, U represents the dimensionless velocity field.

- **Momentum (Navier-Stokes)**

$$\frac{\partial U}{\partial t}+(U . \nabla) U-\nabla P-\nabla . \sigma-\mathbf{F}_{bj}=0 \tag{4}$$

where, t, P and F_{bj} are the time, pressure, and body force per unit mass (buoyancy force), respectively. For the horizontal direction ($j = X$), the body force term $F_{bX} = 0$. On the other hand, for the vertical direction ($j = Y$), the body force term $F_{bY} = Pr\ R\ a \frac{1}{E^2} T_f$.

The nondimensional stress tensor is expressed as:

$$\sigma=2\left[\left(\frac{\mathrm{Pr}}{E}\right) \mathrm{D}-P \mathrm{I}\right] \tag{5}$$

where, I is the identity tensor, and $D = \frac{1}{2}(\nabla U + (\nabla U)^T)$ is rate of deformation (strain rate) tensor.

- Energy in the fluid domain:

$$\frac{\partial T_f}{\partial t}+U . \nabla T_f+\left(\frac{1}{E}\right) . \nabla .\left(-\nabla T_f\right)=0 \tag{6}$$

- Energy in the solid domain (crown region):

$$\frac{\partial T_s}{\partial t}+\alpha_r \nabla .(-\nabla T_s)=0 \tag{7}$$

- Boundary and interface conditions:

To close the mathematical model, the following nondimensional boundary and interface conditions are imposed:

Velocity:

$$U=0 \text{ on all walls and at the interface} \tag{8}$$

Thermal boundary conditions:

Vertical walls (cold):

$$T_f=0 \tag{9}$$

Horizontal walls (adiabatic walls):

$$\nabla T_f=0 \tag{10}$$

Inner surface of the crown (isothermal hot):

$$T_s = 1 \tag{11}$$

Fluid–solid interface conditions (crown outer surface):
Continuity of temperature:

$$T_s = T_f \tag{12}$$

Continuity of heat flux:

$$K_r \left(\frac{\partial T_s}{\partial n} \right)_{solid} = \left(\frac{\partial T_f}{\partial n} \right)_{fluid} \tag{13}$$

where, $K_r = \frac{K_s}{K_f}$ is the thermal conductivity ratio, and n is the unit normal vector at the interface.

This complete nondimensional formulation, coupled with appropriate boundary and interface conditions, provides a robust framework for investigating natural convection and thermal conduction phenomena within geometrically asymmetric enclosures containing an eccentric crown heat source.

2.3 Heat transfer characterization

Convective performance at the solid–fluid interface is assessed using:

- Local Nusselt number:

$$Nu\_Loc = -\frac{\partial T_{sf}}{\partial n}\bigg|_{near\ \text{interface}} \tag{14}$$

where, $\frac{\partial T_{sf}}{\partial n}$ denotes the nondimensional temperature gradient normal to the interface.

- Average Nusselt number:

$$Nu\_avg = \frac{1}{p}\int_s Nu\_Loc\, dS \tag{15}$$

where, P is the perimeter length of the solid–fluid interface, and S denotes the surface area over which the integration is performed.

These indicators quantify the intensity and spatial variation of heat exchange and are crucial for evaluating the impact of eccentricity.

2.4 Thermodynamic assessment

Entropy generation within the fluid domain is assessed based on the second law of thermodynamics, considering two primary dimensionless contributions:

$$N_{total} = N_{heat} + \frac{Br}{E^2} N_{visc} \tag{16}$$

where, N_{heat}, N_{visc} correspond to irreversibility due to heat transfer and viscous dissipation, respectively. The Brinkman number Br is incorporated to account for the effects of viscous dissipation, with a fixed value of $Br = 10^{-3}$ adopted in this study.

The Bejan number Be is used to identify the dominant irreversibility mechanism:

$$Be = \frac{1}{1 + \frac{Br}{E^2} \cdot \frac{N_{visc}}{N_{heat}}} \tag{17}$$

- $Be \simeq 1 \rightarrow$ Heat transfer dominates (thermal irreversibility).
- $Be \simeq 0 \rightarrow$ Viscous dissipation dominates (fluid friction irreversibility).

2.5 Numerical implementation

The Finite Element Method (FEM) is employed to numerically solve the governing Eqs. (3) to (13), with the computational domain discretized using triangular elements to accommodate complex geometries effectively [29]. Within each element, the primary field variables—velocity, pressure, and temperature—are approximated using Lagrange interpolation functions, while Gaussian quadrature is applied to ensure accurate numerical integration [30]. A non-uniform mesh, refined in boundary layer regions, enhances solution accuracy near solid–fluid interfaces and improves computational efficiency. For the thermal field, the heat transfer equation is solved using the implicit Newton–Raphson method, which provides robust stability and reliable convergence in nonlinear scenarios Lorsung and Farimani [31]. Numerical convergence is considered achieved when the residuals for velocity and temperature fall below 10^{-6}, ensuring accuracy and consistency of the results [32].

2.6 Validation and grid sensitivity

To ensure the accuracy and reliability of the numerical results, a mesh independence study was conducted. The test involves monitoring the dimensionless temperature at the point (X = 0.7, Y = 0.5) as a function of dimensionless time, capturing both the transient response and the steady-state behavior. Simulations were carried out using four different mesh densities, as summarized in Table 1. The corresponding results, obtained for Ra = 10^5 and Pr = 0.71, are presented in Figure 3. As illustrated, all four mesh configurations yield identical steady-state temperatures after a brief transient phase, confirming that the solution is not significantly influenced by mesh refinement. Notably, Mesh 3, as shown in Figure 4, provides results nearly identical to those of the finest mesh, thereby offering an optimal trade-off between computational cost and numerical accuracy.

Table 1. Mesh parameters for grid check

Mesh Type	Domain Elements
Mesh 1	1162
Mesh 2	1780
Mesh 3	2260
Mesh 4	7936

Figure 5 presents a rigorous validation of the numerical model through a comparison of the local Nusselt number distribution (Nu_Loc) along the angular position θ (in degrees) at the fluid–solid interface, against the benchmark results reported by Demirdžić et al. [33]. The test scenario

corresponds to a thermally driven flow within an enclosure, where buoyancy-induced natural convection dominates the heat transfer mechanism.

The comparison reveals excellent agreement between the present simulation and the benchmark data. Both profiles exhibit a distinct peak in Nu_Loc at lower angular positions, followed by a gradual decrease as θ increases. This behavior reflects the expected physical mechanism: near the leading edge of the heated boundary, steep thermal gradients result in high local heat transfer rates (high Nu_Loc), whereas farther downstream, the combined effects of thermal diffusion and flow recirculation reduce the heat transfer intensity.

Minor discrepancies observed at certain angular positions can be attributed to differences in numerical schemes, mesh structures, and discretization techniques. While the benchmark was based on a finite volume method with non-orthogonal grids, the present finite element formulation still captures the overall trend with high accuracy, demonstrating the robustness and reliability of the adopted numerical approach.

Additionally, the mesh overlay in Figure 5 highlights the spatial refinement near the curved boundaries, which is crucial for accurately resolving local thermal gradients and minimizing numerical diffusion. This careful grid treatment ensures the fidelity of the Nu_Loc predictions, particularly in regions with sharp gradient variations. The strong correlation with benchmark results confirms the capability of the present method to accurately simulate natural convection phenomena, thus validating its suitability for subsequent parametric analyses and practical engineering applications.

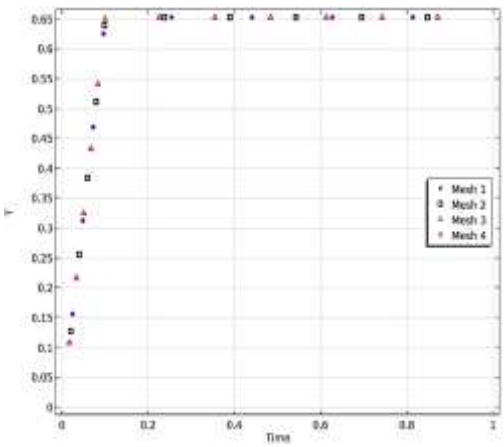

Figure 3. Grid independence test: Temperature evolution at (0.7, 0.5)

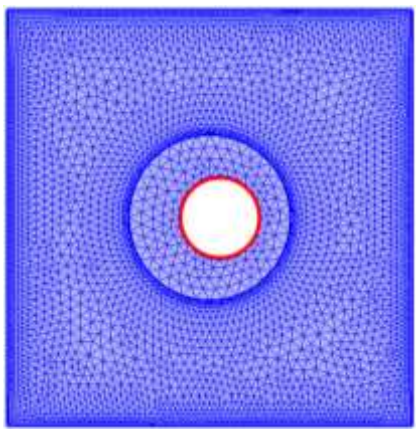

Figure 4. The computational mesh employed, Mesh 3

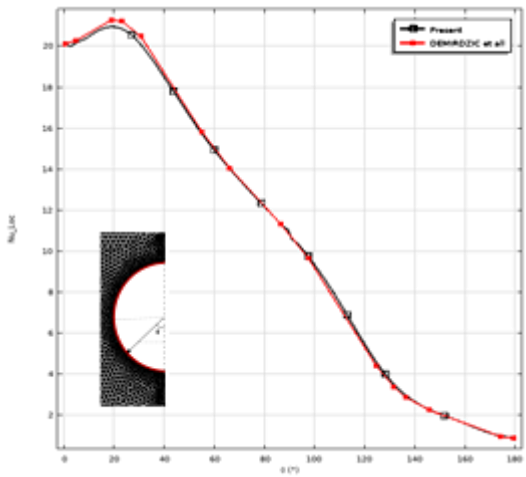

Figure 5. Comparison with Demirdžić et al. [33] in case 4 of a square cavity with a concentric heated cylinder asymmetrically arranged

3. RESULTS AND DISCUSSION

The present analysis provides a comprehensive investigation of coupled thermo-fluid dynamics at the solid–fluid interface by accounting for the realistic thermophysical properties of both domains.

Air is selected as the working fluid (Pr = 0.71), while the heat source is represented by a high-conductivity copper insert with an outer radius of Re = 0.2, consistent with the benchmark configuration proposed by Demirdžić et al. [33].

The system exhibits significant thermal property contrasts, characterized by a thermal diffusivity ratio α_r of approximately 5.18 and an exceptionally high thermal conductivity ratio K_r of about 15,607. This stark difference leads to conduction-dominated heat transfer within the solid and generates steep thermal gradients at the solid–fluid interface, which critically affect the development of the convective boundary layer. The thermo-fluid behavior is explored over a range of Rayleigh numbers Ra = 10^3 - 10^7, with particular emphasis on the influence of geometric asymmetry. This asymmetry is introduced through varying eccentricity ratios (E = 1/4, 1/2, and 1), allowing a detailed assessment of its impact on the overall thermal performance and flow characteristics of the system.

3.1 Flow structure intensity

Figure 6(a)–(c) shows stream function contours for eccentricity ratios E = 1/4, 1/2, and 1, across Ra = 10^3 to 10^7, revealing how eccentric heat source placement alters buoyancy-driven flow dynamics. At Ra = 10^3, the flow is conduction-dominated with weak circulation. ψ_max is low for E = 1/4 and drops by ~8% and ~15% for E = 1/2 and E = 1, due to flow confinement and stagnation zones near the displaced heat source. At Ra = 10^4, buoyancy begins to drive convection. ψ_max increases by ~300% for E = 1/4, with a dominant recirculation cell forming. However, ψ_max decreases by 12% and 19% for E = 1/2 and 1, showing that eccentricity disrupts flow organization. By Ra = 10^5, the impact of eccentricity is clearer. ψ_max for E = 1/4 continues to rise (~600% above its value at Ra = 10^3), but reaches only ~85% and 70% of that value for E = 1/2 and 1, respectively, due to skewed thermal gradients and increased wall resistance.

At Ra = 10^6, ψ_max grows sharply-300% higher than at Ra = 10^5 for E = 1/4, indicating strong convection. However, values remain 15–25% lower for E = 1/2 and 1, highlighting persistent flow disruption caused by geometric asymmetry.

At Ra = 10^7, the flow becomes highly convective with multiple vortex cells. ψ_max peaks for E = 1/4 but is 20% and 35% lower for E = 1/2 and 1. Strong eccentricity (E = 1) leads to chaotic vortices, weakens central flow, and increases localized recirculation, ultimately reducing thermal performance.

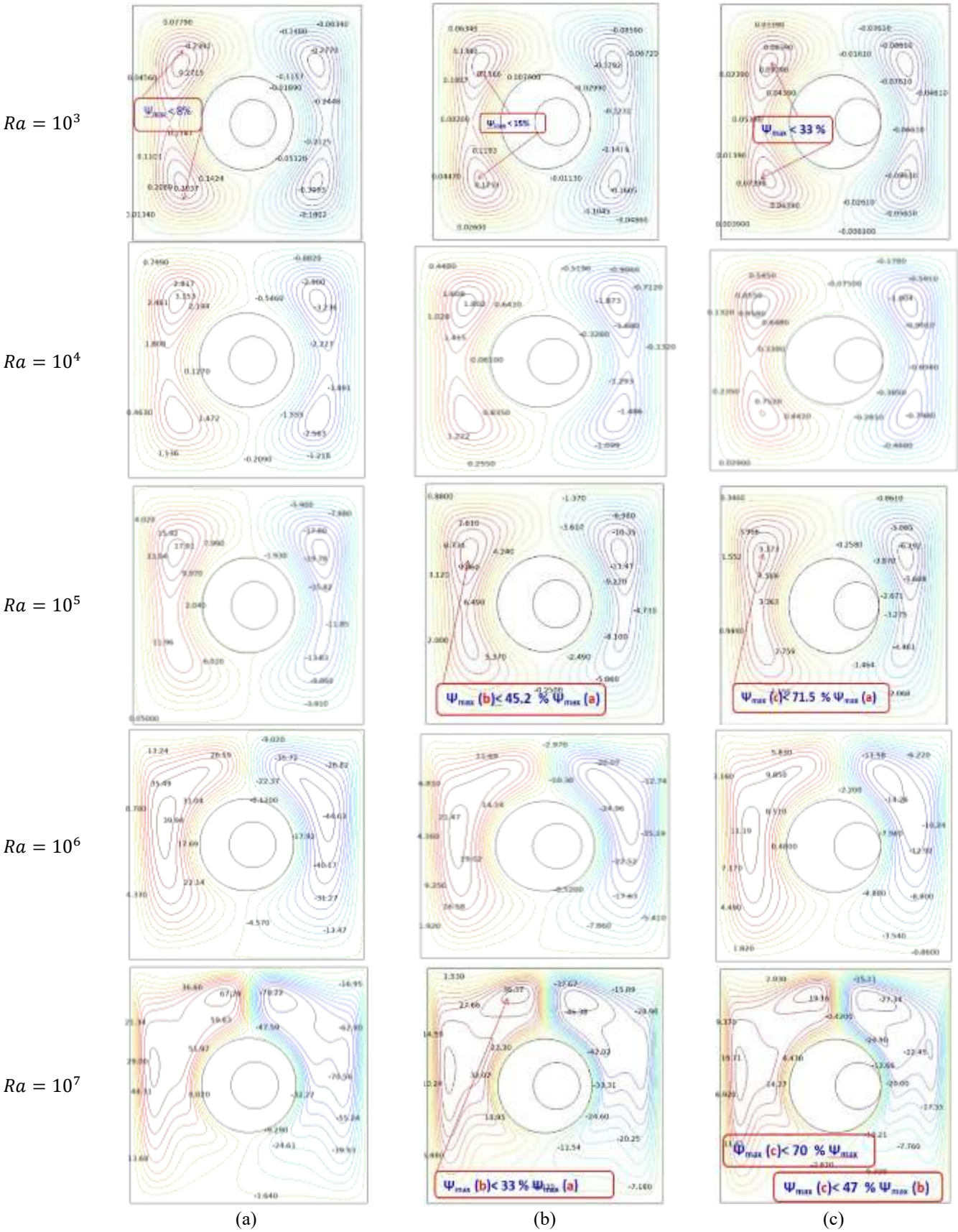

Figure 6. Streamline distributions illustrating the influence of eccentricity (E = 1/4 (a), 1/2 (b), and 1 (c)) on flow structures across Rayleigh numbers $Ra = 10^3 - 10^7$

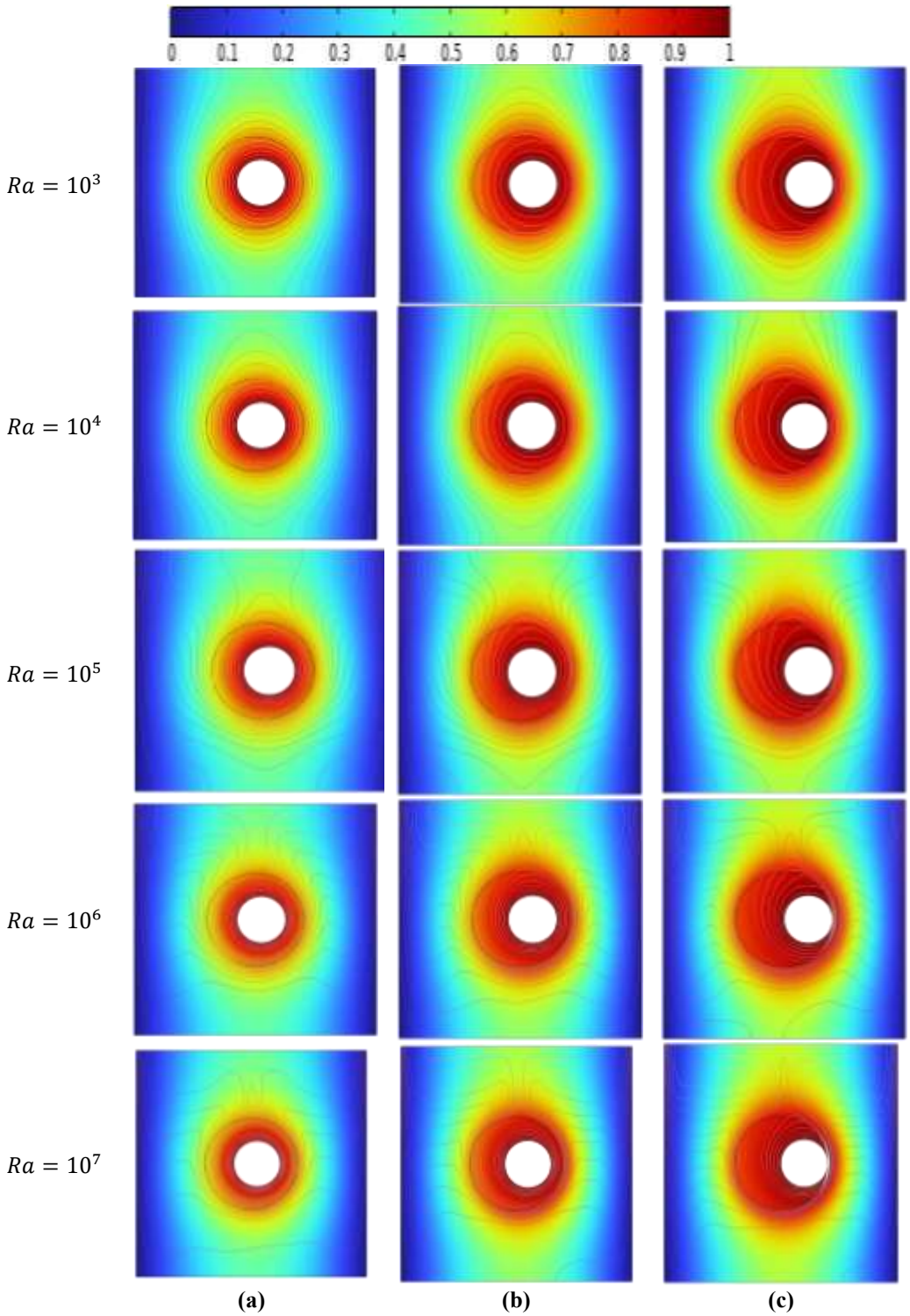

Figure 7. Evolution of isotherm distributions illustrating the influence of eccentricity (E = 1/4 (a), 1/2 (b), and 1 (c)) across Rayleigh numbers $Ra = 10^3 - 10^7$

3.2 Thermal isotherm topology

Figure 7(a)–(c) presents isotherm contours in a square cavity with an eccentric circular heat source for Ra = 10^3 – 10^7 and eccentricities E = 1/4, 1/2, and 1. These contours reveal the transition from conduction to convection and show how eccentricity affects thermal stratification and heat transfer.

At Ra = 10^3, heat transfer is dominated by conduction. Isotherms are nearly concentric for all E values, showing minimal fluid motion. Slight distortions appear for E = 1/2 and 1, especially near the cavity wall, but thermal mixing remains negligible. At Ra = 10^4, weak convection begins. For E = 1/4, isotherms tilt and stretch, showing early buoyant plume development. For E = 1/2 and 1, asymmetries increase—compressed near the heated wall and elongated opposite it—indicating weak, asymmetric convective cells and localized gradients.

At Ra = 10^5, convection strengthens. For E = 1/4, banana-shaped isotherms form a rising plume, enhancing heat transport. For E = 1/2 and 1, the plume is distorted and deflected due to the eccentric source, leading to curved isotherms, stagnation zones, and reduced efficiency. At Ra = 10^6, convection dominates. For E = 1/4, isotherms are vertical and tightly packed, showing strong upward heat transfer. For

E = 1/2 and 1, distortion increases, with isotherms splitting and spreading laterally, reflecting secondary flows and elevated mixing, but also greater thermal resistance due to asymmetry.

At Ra = 10^7, isotherms for E = 1/4 form narrow, vertical jets with steep gradients, indicating high convective efficiency. In contrast, E = 1/2 and 1 show chaotic isotherm fields, sharp bending, and dispersion, highlighting asymmetric vortex activity and reduced heat transfer uniformity—particularly severe for E = 1.

3.3 Local and average numbers analysis

Figure 8 presents the angular distribution of the local Nusselt number along the 0°–360° fluid–solid interface at the outer surface of an eccentric circular crown, for Rayleigh numbers ranging from 10^3 to 10^7 and eccentricity ratios E = 1/4, 1/2, and 1. These profiles offer valuable insights into the evolution of local convective heat transfer mechanisms governed by buoyancy-driven flow within the enclosure. At low Rayleigh numbers (Ra = 10^3), heat transfer is predominantly conduction-driven, as reflected in the relatively flat and symmetric local Nusselt number distributions across all eccentricity ratios. Nonetheless, even at these low Ra values, increasing eccentricity introduces slight asymmetries, shifting the regions of peak heat transfer due to modified thermal gradients around the displaced heat source. As Ra increases to 10^5, buoyancy-induced convection becomes more significant, leading to elevated and spatially varying local Nusselt numbers. In Figure 8(a) (E = 1/4), distinct peaks begin to emerge near 90° and 270°, corresponding to upward and downward convective flow interactions with the interface. Figure 8(b) (E = 1/2) exhibits a broader separation between these peaks, with steeper gradients, while Figure 8(c) (E = 1) reveals highly localized and intensified maxima shifted away from the geometric midlines, driven by complex vortex dynamics and secondary flow structures arising from the enhanced asymmetry. At high Rayleigh numbers (Ra = 10^7), convection completely dominates the heat transfer process, resulting in strongly fluctuating and sharply peaked Nusselt number profiles. The physical interpretation of measuring heat transfer by convection, in its essence, remains crucial in such cases to directly determine the local Nusselt number. This number represents the effectiveness of convective heat transfer compared to pure conduction at a specific location. The higher the local Nusselt number, the greater the convective heat transfer efficiency at that point. The local Nusselt number is also directly related to the heat transfer coefficient, which is often defined by the distance from the leading edge in external flow or the hydraulic diameter in internal flow for the circular shape proposed in the study.

This variation provides a deeper understanding of the flow's hydrodynamic and thermal characteristics.

Heat transfer manifests asymmetrically as the inner circular cavity shifts to the left. Across all cases (a–c), peak values increase substantially by up to 280% in the E = 1 configuration compared to E = ¼, highlighting the pronounced enhancement of localized heat transfer near regions of intense fluid impingement and recirculation. The angular distribution becomes increasingly asymmetric with higher eccentricity, underscoring the critical role of geometric displacement in dictating the formation of high-transfer and stagnation zones. Overall, Figure 8 underscores the coupled influence of the Rayleigh number and eccentricity ratio on local thermal behavior. While increasing Ra amplifies convective transport and intensifies localized heat exchange, greater E redistributes these effects spatially. This interplay offers valuable guidance for thermal management strategies in enclosures where spatially optimized heat removal is required.

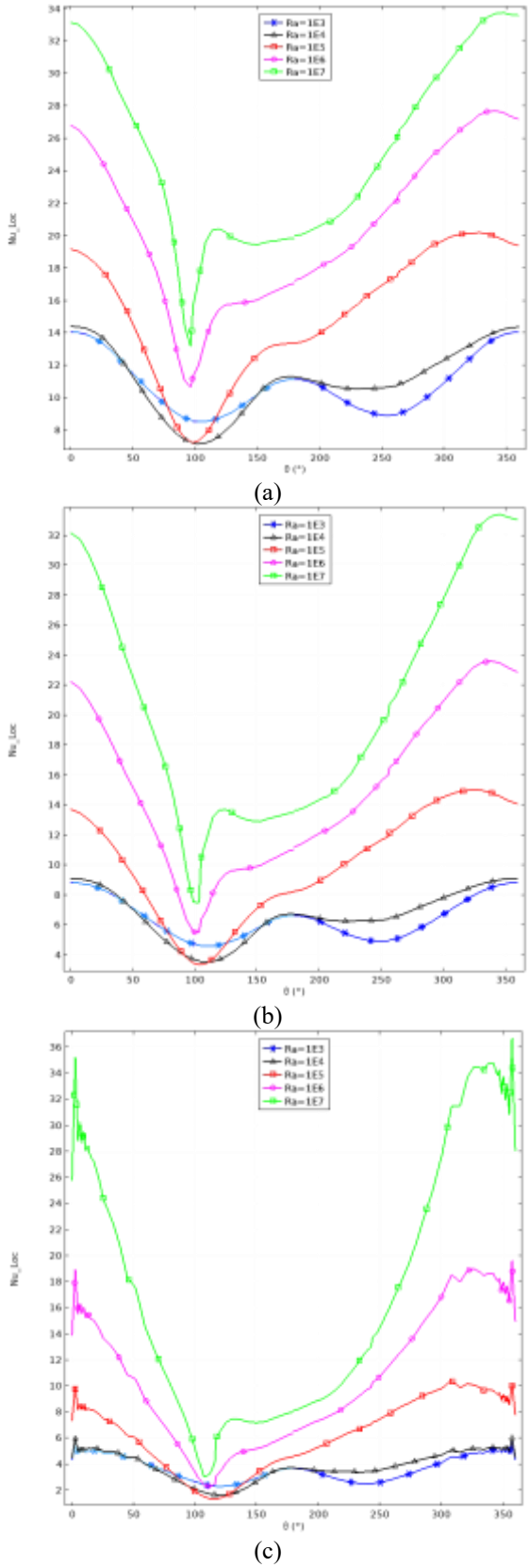

Figure 8. Local Nusselt number profiles along 0°–360° at the fluid-solid interface on the outer surface of an eccentric circular crown for Rayleigh numbers Ra = 10^3 - 10^7 and eccentricity ratios E = 1/4 (a), 1/2 (b), and 1 (c)

Figure 9 examines the effect of eccentricity (E = 1/4, 1/2, and 1) on the average Nusselt number at the fluid–solid interface along the outer surface of an eccentric circular crown, for Rayleigh numbers ranging from 10^3 to 10^7.

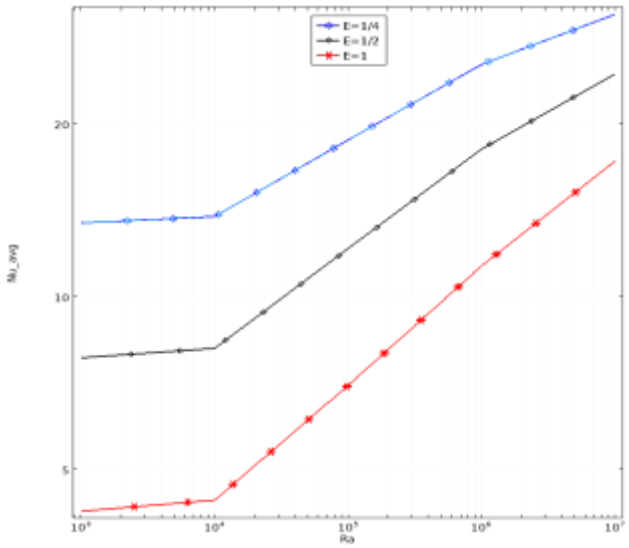

Figure 9. Effect of eccentricity on the average Nusselt number along the fluid–solid interface at the outer surface of an eccentric circular crown for Rayleigh numbers Ra = 10^3-10^7 and eccentricity ratios E = 1/4 (a), 1/2 (b), and 1 (c)

At low Rayleigh numbers (Ra = 10^3), heat transfer is dominated by conduction, and the influence of eccentricity is minimal, with variations in the average Nusselt number remaining below 5%. However, as Ra increases and convective effects become dominant, geometric asymmetry exerts a more pronounced impact on thermal performance. At Ra = 10^5, the average Nusselt number for E = 1/4 is approximately 40% higher than that for E = 1, and this gap widens to nearly 50% at Ra = 10^7. The observed decline in convective efficiency with increasing eccentricity is primarily attributed to the disruption of flow symmetry and the intensification of thermal stratification. These effects hinder the formation of coherent convective cells and reduce overall heat transfer effectiveness. In summary, the results of Figure 9 highlight that increasing eccentricity systematically degrades convective heat transfer. This underscores the importance of geometric optimization in the design of buoyancy-driven thermal systems to enhance thermal performance.

3.4 Entropy generation's impact

Entropy generation plays a crucial role in heat transfer by providing a measure of the irreversibility of a process. In essence, it quantifies how much "disorder" or "randomness" is created during a heat transfer operation.

The second law states that the entropy of an isolated system always increases over time, or remains constant in ideal, reversible processes. In real-world heat transfer, processes are inherently irreversible. Figure 10 presents the angular distribution of the Bejan number along the fluid–solid interface (0°–360°) for different Rayleigh numbers (Ra) and eccentricity ratios (E = 1/4, 1/2, 1) in sub-figures (a), (b), and (c). These profiles reflect how conduction- and convection-induced irreversibilities evolve with changes in Ra and geometric displacement. In Figure 10(a) (E = 1/4), the distribution is nearly symmetric. At low Ra (10^3–10^4), conduction dominates, yielding high Bejan numbers across all angles. As Ra increases (10^5–10^7), buoyancy effects lower the Bejan number, except at 90° and 270°, where persistent peaks mark stagnation zones with high entropy generation. This symmetry indicates stable flow and thermal fields at low eccentricity. In Figure 10(b) (E = 1/2), the Bejan number profile becomes asymmetric. Conduction remains significant at low Ra, but asymmetry increases with Ra, shifting stagnation peaks to around 110° and 250°, due to altered secondary flows that impact recirculation and entropy generation patterns. At E = 1 (Figure 10(c)), strong asymmetry emerges even at low Ra, as the displaced heat source causes skewed conduction irreversibility. At higher Ra, convection dominates, but sharp contrasts persist between low and high Bejan zones. Stagnation peaks appear near 120° and 240°, reflecting enhanced stratification and complex vortices, which increase spatial variations in entropy production. Overall, stagnation zones shift from 90°/270° (E = 1/4) to 120°/240° (E = 1), while higher Ra enhances convection and reduces global entropy generation. However, eccentricity amplifies asymmetry, impacting localized thermal resistance and heat transfer efficiency.

Entropy generation is directly related to the "lost work potential" or "exergy destruction. Heat will flow from a hot object to a cold object. This process is irreversible, and entropy is generated because you can't spontaneously reverse the heat flow without external work. By minimizing entropy generation, designers can optimize heat exchangers, refrigeration cycles, power plants, and other thermal systems to operate more efficiently. Entropy generation arises primarily from heat transfer across a significant temperature difference at angles of 90° and 250°.

An effective enhancement method should increase heat transfer significantly without introducing an excessive amount of irreversibility.

Entropy generation serves as a powerful thermodynamic tool to understand, quantify, and minimize irreversibilities in heat transfer processes. It allows engineers to pinpoint sources of inefficiency and make informed design decisions to improve the performance and sustainability of thermal systems.

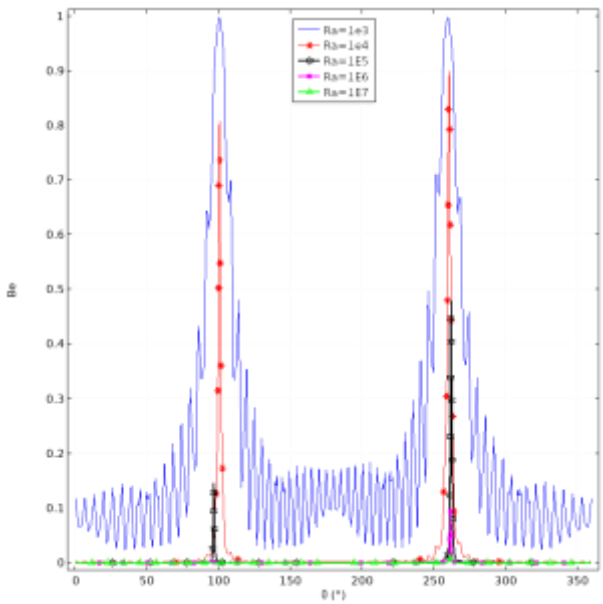

(a)

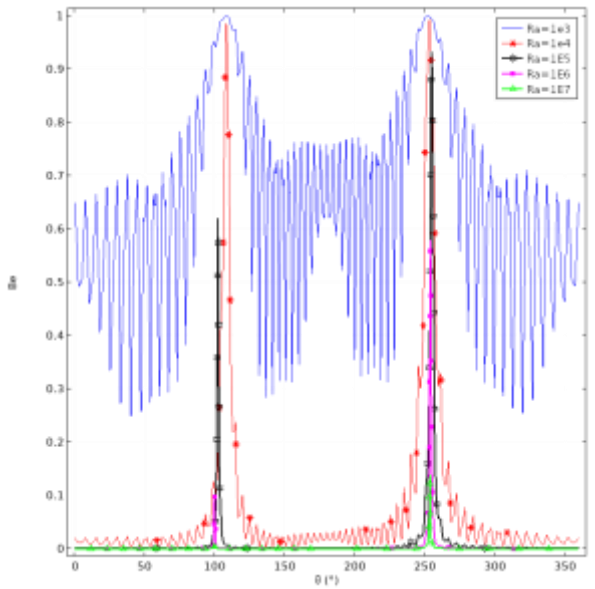

(b)

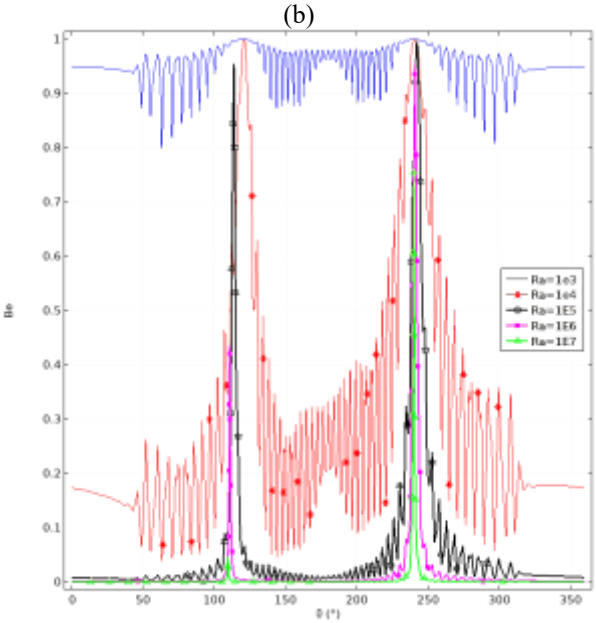

(c)

Figure 10. Influence of eccentricity on the Bejan number distribution at the fluid-solid interface under varying Rayleigh numbers: (a) E = 1/4, (b) E = 1/2, and (c) E = 1

3.5 Empirical correlation

An empirical correlation has been formulated to quantify the combined effects of the Rayleigh number (Ra), Prandtl number (Pr), and eccentricity ratio (E) on the average Nusselt number at the fluid–solid interface along the outer surface of an eccentric circular crown within a square cavity containing a displaced heat source.

The derived correlation takes the following generalized form:

$$Nu\_avg = 6.43.Ra^{(0.19-0.053E)}.\Pr^{0.2}.\left(1-0.5E+0.1E^2\right) \quad (18)$$

This correlation indicates that the heat transfer rate, represented by the Nusselt number, increases with the Rayleigh number (Ra) following a power-law behavior, reflecting the growing dominance of buoyancy-driven convection. However, increasing the eccentricity (E) leads to a reduction in overall heat transfer efficiency, primarily due to the enhanced thermal stratification and disruption of coherent convective flow structures. The proposed correlation thus serves as a reliable predictive tool for evaluating convective heat transfer in enclosures containing eccentric circular crown heat sources, offering practical guidance for the design and optimization of thermally efficient systems in engineering applications.

4. CONCLUSIONS

This numerical study explores conjugate heat transfer and thermo-fluid interactions within a square enclosure containing an eccentric circular copper crown heat source. By varying the Rayleigh number (Ra) and eccentricity ratio (E = 1/4, 1/2, 1), the study examines the coupling between buoyancy-driven flow, conduction in the solid, and natural convection in the fluid.

Results show that geometric eccentricity significantly influences flow strength, structure, and thermal coupling. At moderate eccentricity (E = 1/4), the interface enables efficient heat exchange with coherent vortices and aligned isotherms. However, higher eccentricity E = 1 introduces asymmetries that disrupt the flow, weaken momentum–thermal coupling, and create uneven thermal boundary layers.

At high Ra, convective strength drops by up to 35% for E = 1. Isotherms indicate a shift from conduction-dominated to mixed regimes as Ra increases. Greater eccentricity disturbs thermal pathways, leading to plume bifurcation, stratification, and reduced heat extraction from the solid. These effects also raise local thermal resistance along the eccentric crown surface.

Nusselt number analyses confirm that at high Ra, average values drop by ~50% from E = 1/4 to E = 1. Local Nusselt profiles become asymmetric and concentrated near stagnation zones, revealing uneven thermal loading.

An empirical correlation is proposed to relate Ra, Pr, and eccentricity to the average Nusselt number, capturing the nonlinear decline in convective performance with increasing eccentricity.

This study showed that horizontal eccentric displacement affects the fluid velocity and thus increases the heat load in the studied container.

The variation of the Bejan number proved that a significant temperature difference at angles (from 90° to 110°) and 250°, where shifting stagnation peaks to around 110° and 250°, due to altered secondary flows that impact recirculation and entropy generation patterns. So, the Bejan number for heat transfer might indicate a greater potential for improving thermal design.

The proposed equation remains a significant and important step to measure the combined effects of the Rayleigh number (Ra), the Prandtl number (Pr), and the skewness coefficient (E) on the mean Nusselt number at the liquid-solid interface along the outer surface of an eccentric circular ring inside a square cavity containing a displaced heat source.

In summary, while slight eccentricity can enhance mixing and heat transfer, excessive displacement impairs flow symmetry and boundary layer stability, reducing overall efficiency. These findings stress the importance of geometric optimization at the fluid–solid interface for efficient passive cooling and thermal system design.

REFERENCES

[1] Eid, E.I., Abdel-Halim, M., Easa, A.S. (2015). Effect of opposed eccentricity on free convective heat transfer through elliptical annulus enclosures in blunt and slender orientations. Heat and Mass Transfer, 51(2): 239-250. http:// doi.org/10.1007/s00231-014-1408-z

[2] Wang, S. (1995). An experimental and numerical study of natural convection heat transfer in horizontal annuli between eccentric cylinders. Journal of Thermal Science, 4(1): 38-43. http://doi.org/10.1007/BF02653162

[3] Azzawi, I.D., Hasan, A.F., Yahya, S.G. (2023). Computational optimum design of natural convection in a concentric and eccentric annular cylinder using nanofluids. Proceedings of the Institution of Mechanical Engineers, Part A: Journal of Power and Energy, 237(3): 517-526. http://doi.org/10.1177/09576509221117936

[4] Mota, J.B., Esteves, I.A.A.C., Portugal, C.A.M., Esperança, J.M.S.S., Saatdjian, E. (2000). Natural convection heat transfer in horizontal eccentric elliptic annuli containing saturated porous media. International Journal of Heat and Mass Transfer, 43(24): 4367-4379. http://doi.org/10.1016/S0017-9310(00)00068-5

[5] Gholamalipour, P., Siavashi, M., Doranehgard, M.H. (2019). Eccentricity effects of heat source inside a porous annulus on the natural convection heat transfer and entropy generation of Cu-water nanofluid. International Communications in Heat and Mass Transfer, 109: 104367. http://doi.org/10.1016/j.icheatmasstransfer.2019.104367

[6] Kiwan, S., Alzahrany, M.S. (2007). Effect of using porous inserts on natural convection heat transfer between two concentric vertical cylinders. Numerical Heat Transfer, Part A: Applications, 53(8): 870-889. http://doi.org/10.1080/10407780701715869

[7] Ait Messaoudene, N., Horimek, A., Nouar, C., Benaouda-Zouaoui, B. (2011). Laminar mixed convection in an eccentric annular horizontal duct for a thermodependent non-Newtonian fluid. International Journal of Heat and Mass Transfer, 54(19-20): 4220-4234. http://doi.org/10.1016/j.ijheatmasstransfer.2011.05.022

[8] Yoo, J.S. (1998). Mixed convection of air between two horizontal concentric cylinders with a cooled rotating outer cylinder. International Journal of Heat and Mass Transfer, 41(2): 293-302. https://doi.org/10.1016/S0017-9310(97)00141-5

[9] Guj, G., Stella, F. (1995). Natural convection in horizontal eccentric annuli: numerical study. Numerical Heat Transfer, Part A: Applications, 27(1): 89-105. https://doi.org/10.1080/10407789508913690

[10] Qiao, M., Gao, Z., Li, S., Zhang, H., Xu, F. (2024). Transition of natural convection on a cooled circular surface with heated annular extension. International Communications in Heat and Mass Transfer, 151: 107217. http://doi.org/10.1016/j.icheatmasstransfer.2023.107217

[11] Ashouri, M., Zarei, M.M., Moosavi, A. (2022). Investigation of the effects of geometrical parameters, eccentricity and perforated fins on natural convection heat transfer in a finned horizontal annulus using three dimensional lattice Boltzmann flux solver. International Journal of Numerical Methods for Heat & Fluid Flow, 32(1): 283-312. https://doi.org/10.1108/HFF-10-2020-0629

[12] Taha, M., Ates, A., Altun, A.H., Canlı, E. (2020). Natural convection from perforated vertical fins with different hole diameters. International Journal of Energy Applications and Technologies, 7(4): 154-160. http://doi.org/10.31593/ijeat.850296

[13] Tarek, N., Elhadj, B., Mohammed, H., Khadidja, A. (2023). Numerical simulation of fluid-structure interaction in undulated cavity. International Journal of Heat & Technology, 41(5): 1205-1216. http://doi.org/10.18280/ijht.410511

[14] Al-Mashat, S.M., Othman, T.T., Hamada, K.I. (2007). An experimental study of natural convection heat transfer through a cavity between eccentric horizontal cylinders. Tikrit Journal of Engineering Sciences, 14(2): 57-79. https://doi.org/10.25130/tjes.14.2.07

[15] Yoon, J.S., Shim, Y.J. (2021). Classification of flow modes for natural convection in a square enclosure with an eccentric circular cylinder. Energies, 14: 2788. http://doi.org/10.3390/en14102788

[16] Onochin, J., Jaszczur, M. (2025). Thermal analysis of a borehole heat exchanger with non-concentric pipe configurations. Journal of Physics: Conference Series 3107(1): 012032. http://doi.org/10.1088/1742-6596/3107/1/012032

[17] Yang, L., Farouk, B. (1995). Mixed convection around a heated rotating horizontal square cylinder in a circular enclosure. Numerical Heat Transfer, Part A: Applications, 28(1): 1-18. http://doi.org/10.1080/10407789508913729

[18] Bejan, A., Lorente, S. (2015). Constructal law of design and evolution: Geometry, flow, and performance. Journal of Applied Physics, 113(15): 151301. http://doi.org/10.1063/1.4798429

[19] Parvin, S., Roy, N.C., Saha, L.K., Siddiqa, S. (2022). Heat transfer characteristics of nanofluids from a sinusoidal corrugated cylinder placed in a square cavity. Proceedings of the Institution of Mechanical Engineers, Part C: Journal of Mechanical Engineering Science, 236(5): 2617-2630. https://doi.org/10.1177/09544062211027208

[20] Sheikholeslami, M., Gorji-Bandpy, M., Ganji, D.D. (2018). MHD free convection in an eccentric semi-annulus filled with nanofluid. Journal of the Taiwan Institute of Chemical Engineers, 45(4): 1204-1216. https://doi.org/10.1016/j.jtice.2014.03.010

[21] El-Shaarawi, M.A., Mokheimer, E.M., Jamal, A. (2007). Geometry effects on conjugate natural convection heat transfer in vertical eccentric annuli. International Journal of Numerical Methods for Heat & Fluid Flow, 17(5): 461-493. https://doi.org/10.1108/09615530710752955

[22] Kurnia, J.C., Ghoreishi-Madiseh, S.A., Sasmito, A.P. (2020). Heat transfer and entropy generation in concentric/eccentric double-pipe helical heat exchangers. Heat Transfer Engineering, 41(18): 1552-1575. http://doi.org/10.1080/01457632.2019.1661666

[23] Liu, Y., Tao, Y. (2020). Effect of eccentricity on melting and solidification processes of phase change material inside a shell-and-tube latent heat storage unit. Energy Proceedings, 20: 1-8. https://www.energy-proceedings.org/wp-content/uploads/icae2021/1642952748.pdf.

[24] Boulechfar, H., Djezzar, M., Labed, A. (2015). Effect of eccentricity on natural convection in fluid-saturated

porous media in an elliptical annulus. Mechanics & Industry, 16(4): 403. https://doi.org/10.1051/meca/2015015
[25] Khaoula, B.A., Fayçal, B.N. (2021). Improved energy efficiency of mixed convection heating process in eccentric annulus. Advances in Mechanical Engineering, 13(8): 16878140211039150. http://doi.org/10.1177/16878140211039150
[26] Humaira Tasnim, S., Mahmud, S., Das, P.K. (2002). Effect of aspect ratio and eccentricity on heat transfer from a cylinder in a cavity. International Journal of Numerical Methods for Heat & Fluid Flow, 12(7): 855-869. https://doi.org/10.1108/09615530210443061
[27] Zhang, J., Li, S. (2014). Numerical studies of an eccentric tube-in-tube helically coiled heat exchanger for IHEP-ADS helium purification system. arXiv preprint arXiv:1412.8535. https://doi.org/10.48550/arXiv.1412.8535
[28] Benameur, A., Elmir, M., Mebarki, B. (2022). Numerical simulation by the lattice Boltzmann method of the natural convective flow in a square cavity containing a nanofluid. International Journal of Heat and Technology, 40(5): 1125-1132. http://doi.org/10.18280/ijht.400502
[29] Efendiev, Y., Hou, T.Y. (2009). Multiscale Finite Element Methods: Theory and Applications (Vol. 4). Springer Science & Business Media.
[30] Foti, D., Giorno, S., Duraisamy, K. (2020). An adaptive mesh refinement approach based on optimal sparse sensing. Theoretical and Computational Fluid Dynamics, 34: 457-482. http://doi.org/10.1007/s00162-020-00522-2
[31] Lorsung, C., Farimani, A.B. (2022). MeshDQN: A deep reinforcement learning framework for improving meshes in computational fluid dynamics. arXiv preprint arXiv:2212.01428. https://doi.org/10.48550/arXiv.2212.01428
[32] Zhu, Y., Zhao, S., Zhou, Y., Liang, H., Bian, X. (2024). An unstructured adaptive mesh refinement for steady flows based on physics-informed neural networks. Journal of Computational Physics, 540: 114283 http://doi.org/10.1016/j.jcp.2025.114283
[33] Demirdžić, I., Lilek, Ž., Perić, M. (1992). Fluid flow and heat transfer test problems for non-orthogonal grids: bench-mark solutions. International Journal for Numerical Methods in Fluids, 15(3): 329-354. http://doi.org/10.1002/fld.1650150306

NOMENCLATURE

Nu_Loc	local Nusselt number
E	eccentricity parameter of eccentric cylinders
Ceh	horizontal distance shifted, m
R_e^*	outer tube radius, m
R_i^*	inner radius of the shell, m
R_e	the dimensionless outer radius
R_i	the dimensionless inner radius
g	gravitational acceleration
K	thermal conductivity
L	width of cavity
H	height of cavity
Pr	Prandtl number
Ra	rayleigh number
Be	Bejan number
Br	brinkman number
t	non-dimensional time
T	temperature, K
C_p	specific heat, J/Kg·K
$\boldsymbol{u}^f, \boldsymbol{v}^f$	x- and y- velocity components, m/s
u, v	X- and Y- non-dimensional velocity components
P	dimensionless pressure
Nu_avg	average Nusselt number
x_s	the dimensionless displacement of the fin
T^*	the dimensionless temperature
x , y $\wp$ X , Y	space coordinates, m $\wp$ Dimensionless space coordinates

Greek symbols

α	thermal diffusivity, m^2/s
β	thermal expansion coefficient, l/K
μ	dynamic viscosity, Kg/s
υ	kinematic viscosity, m^2/s
ρ	density, Kg/m^2
$\mathbf{F}_{bY}$	the vertical body force
$\mathbf{F}_{bX}$	the horizontal body force
ψ	Non-dimensional stream function

Subscripts

c	cold
f	fluid
h	hot
r	the solid to the fluid property ratio
s	solid